

Measurement of ω and ϕ meson production via
dimuons at forward rapidity in pp collisions at
 $\sqrt{s} = 13.6$ TeV with ALICE.

Masahiro Oida

Contents

1	Introduction	2
1.1	QCD	2
1.2	Chiral symmetry	3
1.3	NJL model	4
1.4	Quark-Gluon Plasma (QGP)	6
1.5	Heavy Ion collision	7
1.6	Dilepton Measurement[5]	9
1.7	Search for chiral symmetry restoration in QGP	10
1.8	Analysis of pp collision data as a baseline	11
2	Detector setup	13
2.1	Large Hadron Collider (LHC)	13
2.2	A Large Ion Collider Experiment (ALICE)	13
2.2.1	MUON Spectrometer	14
2.2.2	MFT	15
2.2.3	MFT-MUON Track Matching	15
3	Analysis	17
3.1	DataSet	17
3.2	Event selection	17
3.3	Single muon track reconstruction	17
3.4	Single muon selection	18
3.5	Dimuon analysis	18
3.5.1	Dimuon reconstruction	18
3.5.2	Combinatorial background subtraction	19
3.5.3	Peak extraction of $\omega \rightarrow \mu\mu, \phi \rightarrow \mu\mu$	21
3.5.4	Yield calculation of ω, ϕ	21
3.5.5	MFT-MCH matching χ^2 Optimization	23
3.6	Fake Match Track Removal Analysis of MFT-MCH-MID Track using MFT Track η - MCH Track η	23
4	Results	27

1 Introduction

1.1 QCD

The fundamental building blocks of the matter around us are elementary particles. The behavior of elementary particles, such as quarks and gluons, is described by quantum field theory. In particular, quarks and gluons possess a degree of freedom called "color," and the physics governing this degree of freedom is known as Quantum Chromodynamics (QCD). QCD is based on an SU(3) gauge theory and describes the strong interaction. The QCD Lagrangian is expressed as follows:

$$\mathcal{L}_{QCD} = \sum_q \bar{\psi}_{q,a} (i\gamma^\mu \partial_\mu - m_q) \psi_{q,a} + g_s \sum_q \bar{\psi}_{q,a} \gamma^\mu T_{ab}^A \psi_{q,b} G_\mu^A - \frac{1}{4} G_{\mu\nu}^A G^{A\mu\nu} \quad (1)$$

$\psi_{q,a}$ and $\bar{\psi}_{q,a}$ represent the quark and antiquark fields, where q denotes the flavor degree of freedom, and a denotes the color degree of freedom. γ^μ are the gamma matrices, m_q is the particle mass corresponding to each flavor, g_s is the QCD coupling constant, T_{ab}^A are the generator matrices, G_μ^A is the gluon field, and $G_{\mu\nu}^A$ is the gluon field tensor.

The first term in (1) represents the term for a free particle with mass m , the second term describes the interaction between quarks and gluons, and the third term represents the interaction between gluons themselves. A significant difference from Quantum Electrodynamics (QED), which describes electromagnetic interactions, is the presence of the coupling constant $\alpha_s(Q^2)$ and the self-interaction of the gluon field. In QED, the coupling constant does not depend on the energy scale. However, the coupling constant $\alpha_s(Q^2)$ that appears in QCD depends on the energy scale.

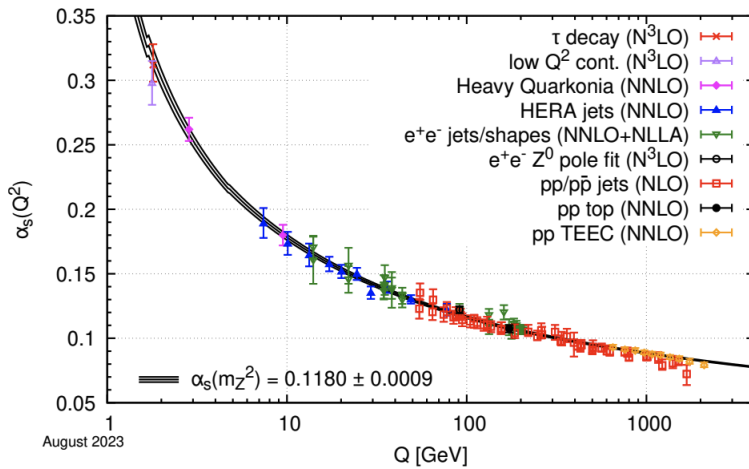


Figure 1: QCD coupling constant[1]

Figure 1 illustrates how the coupling constant $\alpha_s(Q^2)$ changes with the energy scale. At high energy scales, corresponding to short distances, the coupling constant becomes small. This reflects the phenomenon of asymptotic freedom, where quarks behave as

if they are free particles when they are sufficiently close to each other. Conversely, at low energy scales, corresponding to long distances, the coupling constant grows infinitely large. This represents the phenomenon of quark confinement, where quarks cannot be isolated as individual particles.

Next, let us consider the self-interaction of gluons. The gluon field tensor is expressed as:

$$G_{\mu\nu}^A = \partial_\mu G_\nu^A - \partial_\nu G_\mu^A + g_s f^{ABC} G_\mu^B G_\nu^C \quad (2)$$

where f^{ABC} are the structure constants of the SU(3) group. Substituting this into the third term of (1), we obtain:

$$\begin{aligned} -\frac{1}{4} G_{\mu\nu}^A G^{A\mu\nu} &= -\frac{1}{4} (\partial_\mu G_\nu^A - \partial_\nu G_\mu^A + g_s f^{ABC} G_\mu^B G_\nu^C) (\partial^\mu G^{A\nu} - \partial^\nu G^{A\mu} + g_s f^{ABC} G^{B\mu} G^{C\nu}) \\ &= -\frac{1}{4} (\partial_\mu G_\nu^A - \partial_\nu G_\mu^A) (\partial^\mu G^{A\nu} - \partial^\nu G^{A\mu}) \\ &\quad - g_s f^{ABC} G_\mu^B G_\nu^C \partial^\mu G^{A\nu} - g_s^2 f^{ABE} f^{CDE} G_\mu^A G_\nu^B G^{C\mu} G^{D\nu} \end{aligned} \quad (3) \quad (4)$$

In (4), the first term represents the free gluon field without interactions. The second term corresponds to interactions involving three gluon fields, representing reactions such as $g + g \rightarrow g$. The third term corresponds to interactions involving four gluon fields, representing reactions such as $g + g \rightarrow g + g$. For photons, the third term in (2) does not exist, so the second and third terms in (4) do not appear. This is because gluons interact with each other due to their color degrees of freedom, which gives rise to gluon self-interaction.

These characteristics—namely, the energy dependence of the coupling constant and the self-interaction of gluons—contribute to the complex structure of the quark-gluon interactions.

1.2 Chiral symmetry

The quark field is separated into its right-handed and left-handed components. The projection operators for the right-handed and left-handed components are P_R and P_L , respectively. Using the γ matrices, they are expressed as follows:

$$P_R = \frac{1 + \gamma_5}{2}, \quad P_L = \frac{1 - \gamma_5}{2} \quad (5)$$

Their properties are given by:

$$P_R + P_L = 1, \quad P_R P_L = 0, \quad P_R^2 = P_R, \quad P_L^2 = P_L \quad (6)$$

The right-handed quark field q_R and the left-handed quark field q_L are expressed using the projection operators as follows:

$$q_R = P_R q, \quad q_L = P_L q \quad (7)$$

These components are applied to the QCD Lagrangian:

$$\mathcal{L}_{QCD} = \sum_q \bar{q}(i\gamma^\mu D_\mu - m)q \quad (8)$$

Kinetic Term (First Term of the QCD Lagrangian)

$$\bar{q}(i\gamma^\mu D_\mu)q = \bar{q}(i\gamma^\mu D_\mu)(P_R^2 + P_L^2)q \quad (9)$$

$$= \bar{q}P_L(i\gamma^\mu D_\mu)P_Rq + \bar{q}P_R(i\gamma^\mu D_\mu)P_Lq \quad (10)$$

$$= \bar{q}_R(i\gamma^\mu D_\mu)q_R + \bar{q}_L(i\gamma^\mu D_\mu)q_L \quad (11)$$

Mass Term (Second Term of the QCD Lagrangian)

$$\bar{q}mq = \bar{q}m(P_R^2 + P_L^2)q \quad (12)$$

$$= \bar{q}P_RmP_Rq + \bar{q}P_LmP_Lq \quad (13)$$

$$= \bar{q}_Lmq_R + \bar{q}_Rmq_L \quad (14)$$

From the above, the kinetic term of the quark field can be separated into the right-handed and left-handed quark fields, thereby preserving chiral symmetry. However, the mass term mixes the right-handed and left-handed quark fields, breaking chiral symmetry. Considering the chiral limit ($m_q = 0$), the QCD Lagrangian preserves chiral symmetry.

The order parameter for the spontaneous breaking of chiral symmetry is represented by the quark condensate $\langle \bar{q}q \rangle$. As shown in 2, this quantity takes a finite value in the ground state of hadrons at standard temperature and density but is expected to approach $\langle \bar{q}q \rangle \sim 0$ at extremely high temperatures and densities.

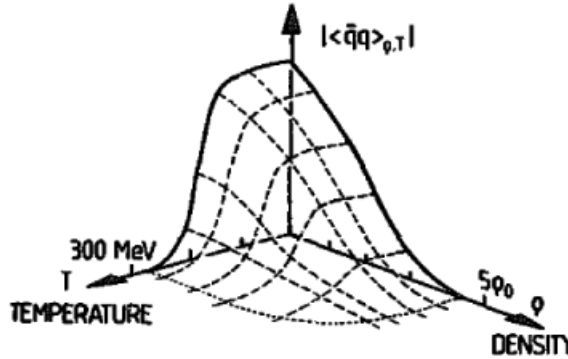


Figure 2: Chiral condensate[2]

Since the vacuum expectation value of the quark condensate cannot be directly measured, as described later, various other probes are used to investigate the restoration of chiral symmetry.

1.3 NJL model

The interaction between quarks and gluons, as described in 1.1, exhibits a complex structure, making it difficult to understand various phenomena from first-principle calculations.

Therefore, models are employed to describe these phenomena. One such model is the Nambu-Jona-Lasinio (NJL) model, a chiral effective model. Its Lagrangian is expressed as follows:

$$\mathcal{L} = \bar{q}i\gamma \cdot \partial q - (-g)[(\bar{q}q)^2 + (\bar{q}i\gamma_5 q)^2] \quad (15)$$

Here, q and \bar{q} represent quark and antiquark fields, respectively; γ and γ_5 are gamma matrices, with $\gamma_5 = i\gamma_0\gamma_1\gamma_2\gamma_3$. Since there is an attractive force between quarks and antiquarks, the coupling constant g is positive and has a dimension of [mass] $^{-2}$. This model serves as a chiral effective theory for QCD at the energy scale of 1 GeV. To determine the ground state of this Lagrangian, the self-consistent mean-field approximation (MFA) is employed:

$$\langle \bar{q}q \rangle \equiv \frac{-m_0^2\sigma}{G} \quad (16)$$

$$\langle \bar{q}i\gamma_5 q \rangle \equiv \frac{-m_0^2\pi}{G} \quad (17)$$

By substituting (16) and (17) into (15), the expression is reformulated. Defining $\sigma = \bar{q}q$, $\pi = \bar{q}i\gamma_5 q$, and $2g = (G/m_0)^2$, we have:

$$\mathcal{L}_{MFA} = \bar{q}[i\gamma \cdot \partial - G(\sigma + i\pi\gamma_5)]q - \frac{m_0^2}{2}(\sigma^2 + \pi^2) \quad (18)$$

Here, defining $q_\theta = e^{i\gamma_5 \frac{\theta}{2}}q$, $G\sqrt{\sigma^2 + \pi^2} = M$, and $\pi/\sigma = \tan\theta$, the Hamiltonian can be expressed as follows. θ is the parameter of the chiral transformation.

$$H_{MFA} = \int d^3x \left\{ \bar{q}_\theta(x)(-i\gamma \cdot \nabla + M)q_\theta(x) + \frac{m_0^2}{2}\sigma_0^2 \right\} \quad (19)$$

Where $\sigma_0^2 = \sigma^2 + \pi^2$. Since π is considered sufficiently small, we write σ to σ_0 . From this Hamiltonian, the Dirac equation for mass M can be derived. Its solution is given as:

$$q_\theta(x) = \frac{1}{\sqrt{V}} \sum_{\mathbf{p}, r=\pm} \sqrt{\frac{M}{E_p}} \left\{ a_M(\mathbf{p}, r)u_M(\mathbf{p}, r)e^{-ip \cdot x} + b_M^\dagger(\mathbf{p}, r)v_M(\mathbf{p}, r)e^{ip \cdot x} \right\} \quad (20)$$

Here, r represents helicity, $E_p = \sqrt{\mathbf{p}^2 + M^2}$, and $M = -g \langle \bar{q}_\theta q_\theta \rangle$. Next, when $q_\theta(x)$ is expanded using spinors with zero mass, the solution is:

$$q_\theta(x) = \frac{1}{\sqrt{V}} \sum_{\mathbf{p}, s=R,L} \left\{ a_{\mathbf{p}}^{(s)}(t)u_0(\mathbf{p}, s)e^{-i\mathbf{p} \cdot \mathbf{x}} + b_{\mathbf{p}}^{(s)\dagger}(t)v_0(\mathbf{p}, s)e^{i\mathbf{p} \cdot \mathbf{x}} \right\} \quad (21)$$

Where s represents helicity. Using the solutions (20) and (21), the Hamiltonian (19) can be expressed in terms of operators for massive and massless states. Here, $a_{\mathbf{p}}$ and $b_{\mathbf{p}}$ are expansion coefficients:

$$H_{MFA} = \sum_{\mathbf{p}, s} \left\{ |\mathbf{p}|(a_{\mathbf{p}}^{(s)\dagger}(t)a_{\mathbf{p}}^{(s)}(t) - b_{-\mathbf{p}}^{(s)}(t)b_{-\mathbf{p}}^{(s)\dagger}(t)) + M(b_{-\mathbf{p}}^{(s)}(t)a_{\mathbf{p}}^{(s)}(t) + a_{\mathbf{p}}^{(s)\dagger}(t)b_{-\mathbf{p}}^{(s)\dagger}(t)) \right\} + V \frac{m_0^2}{2} \sigma_0^2 \quad (22)$$

$$= \sum_{\mathbf{p}, r} E_p \left(a_M^\dagger(\mathbf{p}, r) a_M(\mathbf{p}, r) - b_M(\mathbf{p}, r) b_M^\dagger(\mathbf{p}, r) \right) + V \frac{m_0^2}{2} \sigma_0^2 \quad (23)$$

From this Hamiltonian, the following Heisenberg equation can be derived:

$$i \begin{pmatrix} \dot{a}_{\mathbf{p}}^{(s)}(t) \\ \dot{b}_{-\mathbf{p}}^{(s)}(t) \end{pmatrix} = \begin{pmatrix} |\mathbf{p}| & M \\ M & -|\mathbf{p}| \end{pmatrix} \begin{pmatrix} a_{\mathbf{p}}^{(s)}(t) \\ b_{-\mathbf{p}}^{(s)}(t) \end{pmatrix} \quad (24)$$

Setting the initial condition $a_{\mathbf{p}}^{(s)}(t = 0) = a_{M=0}(\mathbf{p}, s)$, the solution reveals that the massive and massless operators are connected via the Bogoliubov-Valatin transformation:

$$\begin{pmatrix} a_M(\mathbf{p}, r) \\ b_M(\mathbf{p}, r)^\dagger \end{pmatrix} = U(\mathbf{p}, r) \begin{pmatrix} a_0(\mathbf{p}, r) \\ b_0(\mathbf{p}, r)^\dagger \end{pmatrix} U^\dagger(\mathbf{p}, r) \quad (25)$$

Where $U(\mathbf{p}, r) = \exp \left\{ -\frac{\theta_p}{2} (a_0^\dagger(\mathbf{p}, r) b_0^\dagger(-\mathbf{p}, r) - b_0(-\mathbf{p}, r) a_0(\mathbf{p}, r)) \right\}$.

The vacuum states for each operator are defined as follows:

$$|\sigma_0\rangle \rightarrow a_M(\mathbf{p}, r) |\sigma_0\rangle = b_M(\mathbf{p}, r) |\sigma_0\rangle = 0 \quad (26)$$

$$|0\rangle \rightarrow a_0(\mathbf{p}, r) |0\rangle = b_0(\mathbf{p}, r) |0\rangle = 0 \quad (27)$$

$a_0(\mathbf{p}, r)^\dagger$ creates an eigenstate of chirality, while $a_M(\mathbf{p}, r)^\dagger$ creates an eigenstate of helicity. Based on the vacuum definition and (25), acting on $|0\rangle$ produces an eigenstate of helicity but not a definite chirality eigenstate. This implies that "chiral symmetry is spontaneously broken."

Thus, the NJL model theoretically predicts vacuum phase transitions. In our universe, it is believed that quark condensation spontaneously breaks chiral symmetry, leading to hadrons acquiring significant masses.

1.4 Quark-Gluon Plasma (QGP)

When hadrons are subjected to extremely high temperatures and densities, they transition into a plasma state known as the Quark-Gluon Plasma (QGP). In the QGP state, quarks are liberated from confinement, and the restoration of chiral symmetry is also expected.

Furthermore, it is believed that the universe immediately following the Big Bang—just a few tens of microseconds after—was in a QGP state. On the QCD phase diagram, which represents the phase structure of quarks and gluons, the QGP phase appears as shown in Figure 3.

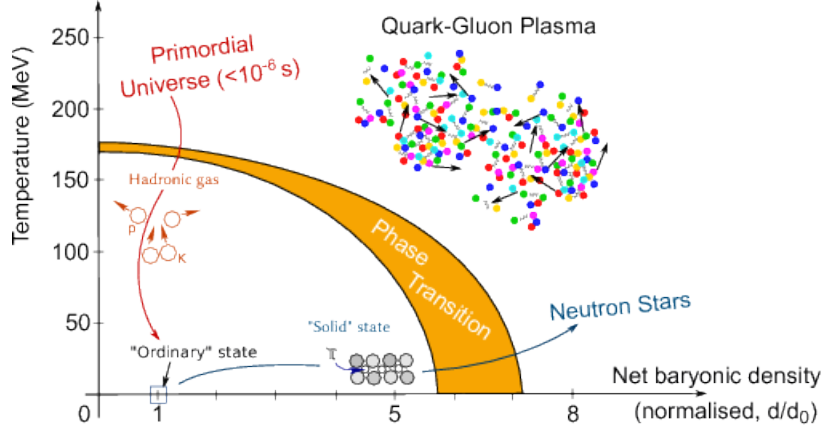


Figure 3: QCD Phase Diagram[3]

The vertical axis, T , represents temperature, while the horizontal axis denotes baryon number density. The world we inhabit belongs to the hadronic phase. In the hadronic phase, quarks acquire a large effective mass due to the spontaneous breaking of chiral symmetry, and they cannot be extracted individually due to confinement.

The QGP phase can be observed in high-temperature regions in both high-density and low-density areas. Two types of phase transitions are involved in the transition to the QGP phase. The first is the chiral phase transition. The second is the deconfinement-confinement phase transition.

The chiral phase transition involves the spontaneous breaking of chiral symmetry as the vacuum undergoes a phase transition, allowing quarks to acquire a substantial effective mass. In other words, the chiral phase transition is deeply related to the mass acquisition of hadrons.

The deconfinement-confinement phase transition pertains to the confinement of quarks. In the hadronic ground state, quarks are confined by the color interaction. However, in the QGP state, quarks are liberated from confinement and transition into a plasma state. This is the deconfinement-confinement phase transition. While these transitions are believed to occur at approximately the same critical temperature, this relationship is not self-evident, and research is still ongoing.

1.5 Heaby Ion collision

The Quark-Gluon Plasma (QGP) as an Ultrahigh Temperature and Density Matter

The existence of the Quark-Gluon Plasma (QGP), an ultrahigh temperature and density state of matter, has been confirmed through heavy-ion collision experiments. QGP

is produced during the temporal evolution of heavy-ion collisions. As shown in Figure 4, the time evolution proceeds in the following sequence:

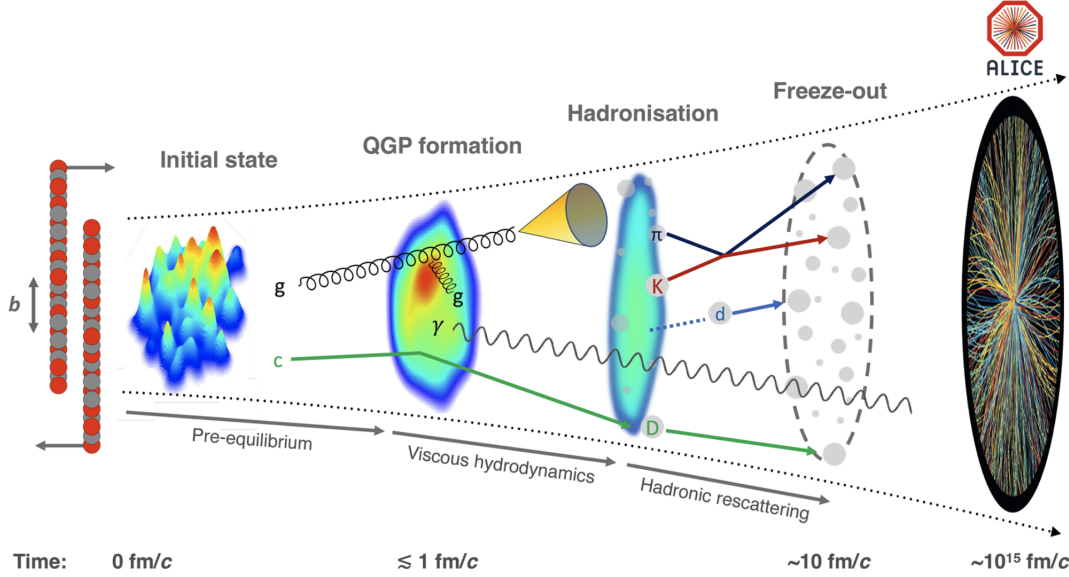


Figure 4: The evolution of a heavy-ion collision at LHC energies[4]

1. Pre-equilibrium state
2. QGP
3. Hadronization
4. Kinetic Freeze-out

In the initial stage of the collision, partons from the nucleons undergo elastic and deeply inelastic scatterings to reach thermalization. During this initial collision, phenomena such as jet production and the pair production of heavy quarks occur. Once the material generated in the collision region reaches thermal equilibrium, the system transitions into the QGP state.

In the QGP state, photons and lepton pairs originating from thermal radiation of high-temperature matter are generated. Jets interact with the QGP and lose energy, resulting in jet quenching, while heavy quarks undergo deconfinement due to the color Debye screening. Subsequently, as the QGP cools, hadronization occurs, leading to chemical freeze-out.

Chemical freeze-out refers to the cessation of changes in particle species due to deeply inelastic scatterings among particles. However, elastic scatterings between hadrons continue, allowing momentum exchange among particles. Later, kinetic freeze-out occurs, fixing the momenta and other properties of the particles. The particles ultimately detected are those that remain after the kinetic freeze-out. Thus, QGP is formed during the temporal evolution of heavy-ion collisions, and its lifetime is extremely short.

The QGP generated in heavy-ion collisions has its density and temperature determined by the collision energy. High-density QGP regions are realized at collision energies of $\sqrt{s_{NN}} \lesssim 10$ [GeV]. At these energies, the colliding particles come to rest at the collision point, creating a high-density state where kinetic energy is converted directly into heat, increasing the temperature.

On the other hand, high-temperature, low-density regions are achieved at collision energies of $\sqrt{s_{NN}} \gtrsim 100$ [GeV]. In this energy regime, the colliding particles do not stop but pass through each other, producing a large number of particle pairs. As a result, the baryon number density does not become large relative to the temperature. However, near the collision point, a high energy density remains, leading to the creation of high-temperature matter.

In the ALICE experiment, LHC Run 3 operations began in 2022, initiating Pb-Pb collision measurements at $\sqrt{s_{NN}} = 5.36$ TeV. This collision energy produces QGP in the ultrahigh temperature, low-density region. Moreover, compared to the QGP generated at $\sqrt{s_{NN}} = 200$ GeV at RHIC, the higher collision energy at LHC enables the measurement of a larger QGP system than ever before.

1.6 Dilepton Measurement[5]

Dilepton measurement is considered a probe to elucidate the temporal evolution of heavy-ion collisions. Leptons do not undergo strong interactions, making them less affected by the QGP. This characteristic allows for the measurement of a distribution that sums up dileptons from all stages of heavy-ion collisions. The sources of dilepton production are as follows:

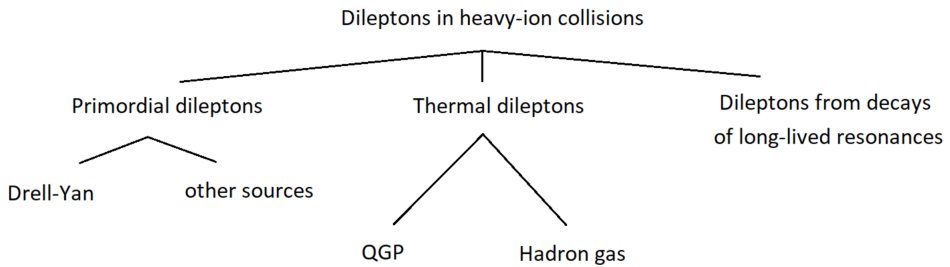


Figure 5: Dilepton source

- Primordial dileptons (from $q\bar{q}$ annihilation)
- Thermal dileptons
- Dileptons from hadron decays

These dileptons correspond to the temporal evolution of heavy-ion collisions through their mass regions.

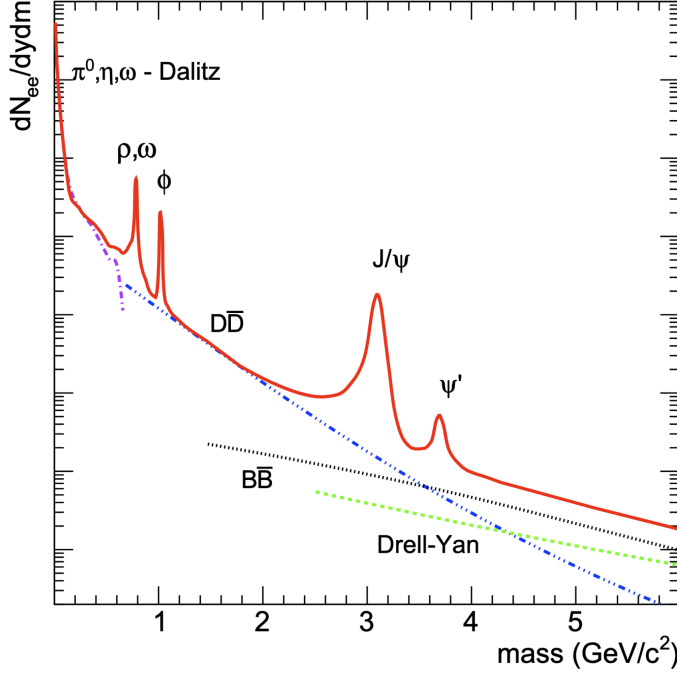


Figure 6: Expected mass spectrum from dileptons[7]

In the High-Mass Region, primordial dileptons (Drell-Yan) constitute the continuum component of the mass distribution, reflecting the initial state of the collision. In the Intermediate-Mass Region, thermal dileptons originating from the QGP, in addition to continuum components such as open-charm and open-beauty, are observed. By measuring thermal dileptons in this mass region, the initial temperature of the QGP can be investigated.

Finally, in the Low-Mass Region, the dilepton distribution is predominantly derived from light meson decays from the hadronic gas. Most dileptons from hadron decays have longer lifetimes compared to the QGP, so the mesons observed in this region are mostly from the hadron gas. However, light vector mesons (ρ, ω, ϕ) have extremely short lifetimes, making them uniquely susceptible to the influence of the QGP compared to other components.

1.7 Search for chiral symmetry restoration in QGP

In the QGP, it is expected that an ultra-high temperature and high-density state is realized, leading to $\langle \bar{q}q \rangle \sim 0$ and the restoration of chiral symmetry. Light vector mesons (ρ, ω, ϕ) serve as probes for the masses of hadrons in the QGP. These particles have short lifetimes and decay channels into dileptons. As illustrated in Fig. 7, their short lifetimes make it possible for them to decay within the QGP, which would otherwise immediately hadronize. Additionally, since they decay exclusively into dileptons, which do not undergo strong interactions with the QGP, the masses of hadrons within the QGP can be measured.

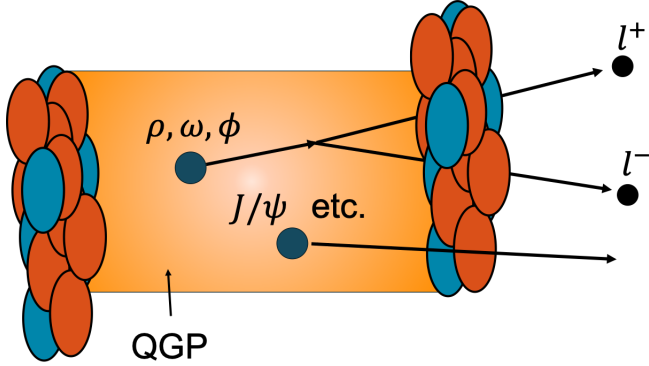


Figure 7: Low mass vector meson decay in QGP

In past experiments, the restoration of chiral symmetry was investigated using dileptons. In the SPS-NA60 experiment, an excess production of electron pairs in the low mass region was reported. However, the excess could also be explained by $\pi + \pi \rightarrow \rho \rightarrow \pi\pi$, and thus it did not serve as definitive evidence of chiral symmetry restoration[8].

Additionally, in the electron pair measurements during ALICE Run 2 $\sqrt{s_{NN}} = 5.02$ TeV PbPb collisions, contributions from open-charm and open-beauty were estimated along with the vacuum dilepton distribution excluding ρ , and an excess of electron pairs was reported. However, the excess was explained as thermal dileptons from the QGP within the error range, and thus chiral symmetry restoration was not definitively demonstrated[6].

This study aims to measure the mass modification of light vector mesons in the QGP using forward muon pairs in ALICE Run 3 $\sqrt{s_{NN}} = 5.36$ TeV PbPb collisions. Starting from ALICE Run 3, the MFT was introduced into the forward detector system of the ALICE experiment, enabling more precise measurements of muon production points compared to Run 2, as well as measurements of muons with lower transverse momentum. By utilizing the differences in muon production points, heavy flavor (HF), which is one of the backgrounds in light vector meson measurements, can be removed. This will allow the measurement of the mass distribution of low transverse momentum light vector mesons, which are more likely to decay within the QGP.

1.8 Analysis of pp collision data as a baseline

This paper presents the analysis results of proton-proton collision events. The particles generated in proton-proton collisions are produced from the vacuum. Measurements of collision events where QGP is not produced serve as a baseline for comparison with events where QGP is generated. Muon analysis using tracks, including the MFT introduced in ALICE Run 3, is being carried out simultaneously with the data acquisition for proton-proton collisions. Currently, the quality of track reconstruction is still insufficient, and the muon pair analysis is also incomplete. Furthermore, the quality of muon tracks in heavy-ion collisions is more challenging than in proton-proton collisions due to the large

number of particles generated in each event.

The objective of this research is to provide an analysis as a baseline for future studies of $\sqrt{s_{NN}} = 5.02$ PbPb collisions, where QGP is expected to be generated, and to improve the quality of muon tracks in ALICE Run 3 $\sqrt{s_{NN}} = 13.6$ TeV pp collisions.

2 Detector setup

2.1 Large Hadron Collider (LHC)

The Large Hadron Collider (LHC) is the world's largest circular accelerator. As shown in Figure 8, the LHC and its major experimental groups are located near Geneva, Switzerland. LHC Run 1 was conducted from 2009 to 2013, and Run 2 took place from 2015 to 2018. The ongoing Run 3 is scheduled to collect physics data from 2022 to the summer of 2026. During the run, most of the periods involve proton-proton collision measurements, with heavy-ion collision measurements conducted for about one month each year. The LHC accelerator hosts four major experimental groups: ATLAS, CMS, LHCb, and ALICE.

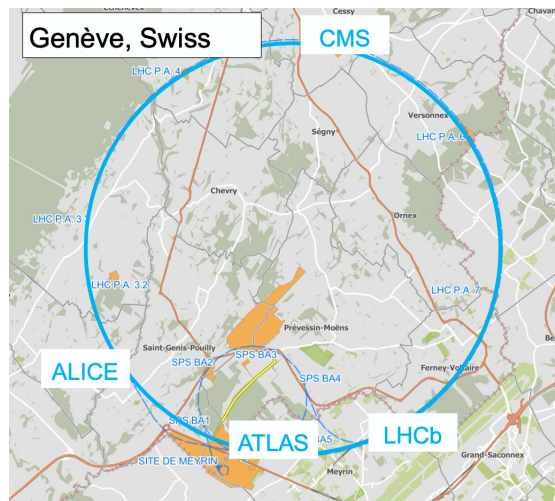


Figure 8: LHC

2.2 A Large Ion Collider Experiment (ALICE)

The ALICE collaboration is an international collaboration consisting of 168 research institutions from 40 countries and around 2,000 researchers. The ALICE detector system is dedicated to research related to the Quark-Gluon Plasma (QGP) produced in heavy-ion collisions. The detectors can be broadly divided into two main groups: the barrel detector group and the forward detector group. The barrel detector group includes detectors such as ITS, TPC, TOF, EMCAL, TRD, PHOS/CPV, and HMPID. A magnetic field is applied along the beam axis, bending the motion of charged particles and enabling particle identification, momentum, and energy measurements. The forward detector group is specifically designed for muon measurements and consists of three trackers—MFT, MCH, and MID—and two hadron absorbers. A dipole magnet is placed between MCH, allowing the measurement of muon momentum and sign. Other detectors include ZDC and FIT. The ZDC is placed far forward of the collision point and measures the number of neutrons

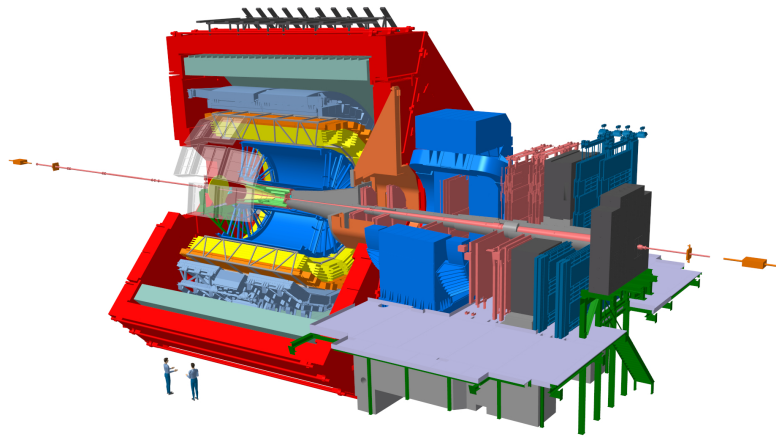


Figure 9: ALICE detectors

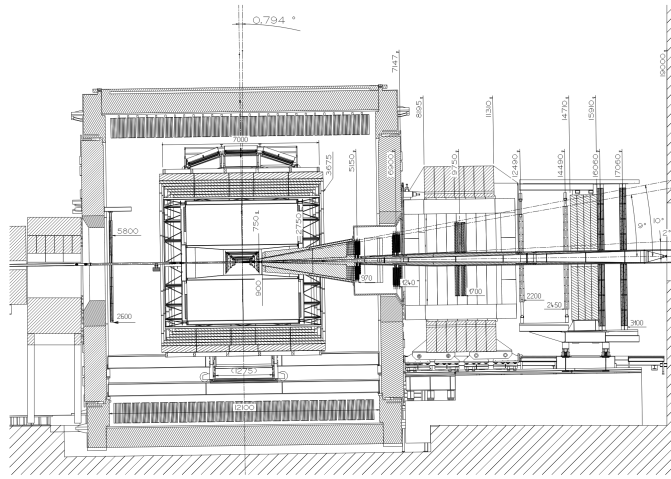


Figure 10: MUON spectrometer

and protons, determining the centrality of heavy-ion collision events. The FIT detectors are placed both forward and backward and are used for measuring event luminosity and particle multiplicity.

2.2.1 MUON Spectrometer

The MUON spectrometer consists of the Front Absorber, MCH, Iron Wall, and MID, and has an acceptance range of $-4.0 < \eta < -2.5$. It uses the high penetration power of muons to identify them. Various particles generated at the collision point (IP) pass through the Front Absorber. Hadrons and light electrons, which interact strongly, are absorbed by the Front Absorber, while muons, due to their high penetration power, pass through it. The muons that pass through the Front Absorber are detected, and any particles such as π mesons that are produced from interactions within the Front Absorber are measured by the MCH. These particles are then absorbed in the Iron Wall, so they are not detected by the MID. Therefore, muon identification (PID) is performed by combining

tracks measured in the MCH and MID. The momentum of the muons is measured using a dipole magnet in the MCH, which is set at a magnetic flux density of 3.0T.

2.2.2 MFT

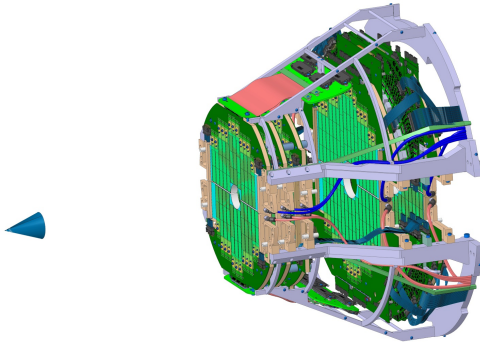


Figure 11: MFT

The MFT is a newly introduced silicon pixel detector in Run 3, installed between $z = 0$ and $z = -76.8$ cm (with an acceptance range of $-3.6 < \eta < -2.5$). It consists of 5 layers of disks that detect tracks and reconstruct MFT standalone tracks considering the influence of the L3 magnet, which creates the ALICE central magnetic field. Since the detector is placed in front of the Front Absorber, the tracks measured include not only muons but also various other particles such as π mesons and kaons. By combining these tracks with those measured by the backward MUON spectrometer, it is possible to measure the DCA of the muons. The ability to measure DCA enables the separation of c and b quarks based on differences in lifetime. Additionally, the precision of the opening angle of the muon pair is improved, which enhances mass resolution. Furthermore, since the MFT is placed in front of the Front Absorber, it allows for the measurement of lower transverse momentum muons compared to those measured by the MUON spectrometer alone.

2.2.3 MFT-MUON Track Matching

The tracks measured by the MUON spectrometer and MFT are matched to reconstruct the Global Track. First, the tracks measured by the MUON spectrometer are extrapolated toward the collision point up to the last disk of the MFT, located at $z = 76.8$ cm. The extrapolation accounts for multiple scattering and energy loss corrections in the hadron absorber between the MUON spectrometer and MFT. Then, suitable MFT tracks are selected based on both position and direction, and the matching quality is evaluated by comparing the position and slope of the tracks. The best quality MFT track is selected and used to construct the Global Track.

Here is the translation of your provided text:

—

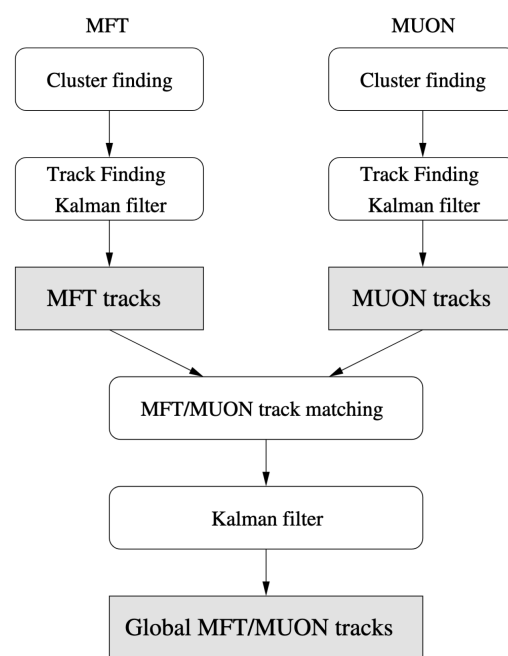


Figure 12: Global Track[9]

3 Analysis

3.1 DataSet

The data used is part of the 500 kHz pp collisions at $\sqrt{s} = 13.6$ TeV, obtained in 2022. The dataset name is LHC22o_apass7. The data from the Monte Carlo simulation used in 3.6 was generated using PYTHIA8 for the 500 kHz pp collisions at $\sqrt{s} = 13.6$ TeV with minimum bias (MB) event simulations.

3.2 Event selection

The position of the proton-proton collision was measured by the ITS detector system. The Z-coordinate of the collision point, denoted as $VtxZ$, was selected with the condition $|VtxZ| < 10$ cm, using the ITS center at $Z = 0$ as the reference. This cut value is aligned with the ITS acceptance. The number of events obtained with this cut is 5.5×10^9 .

3.3 Single muon track reconstruction

The physical quantities of the Global Track, obtained from 2.2.3, were not computed from the quantities of the reconstructed Global Track, but rather using the η, ϕ of the MFT standalone Track and the momentum p from the MCH Track, which were used to reconstruct the Global Track. This recalculation method improves the resolution of p_T, η, ϕ of the track because it uses the η, ϕ of the MFT tracks, which are not influenced by the front absorber, and the momentum p from MCH, which has higher accuracy. Additionally, values such as DCA and R_{abs} were calculated from the Global Track as follows. DCA refers to the distance described in 13. First, the Global Track is linearly extrapolated to the Z-coordinate of the collision point (IP). Then, the distance between this extrapolated position and the collision point is calculated as the DCA. Furthermore, R_{abs} refers to the distance described in Figure 14. The distance from the beam axis to the rear edge of the absorber for the reconstructed Global Track was calculated as R_{abs} .

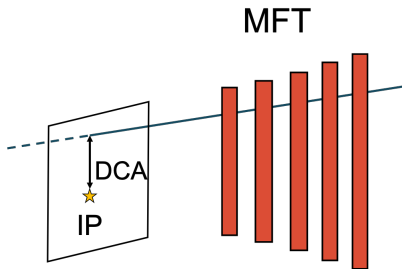


Figure 13: DCA

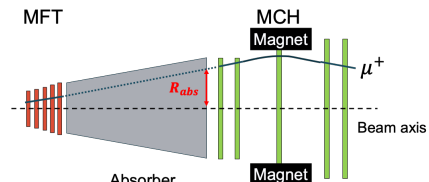


Figure 14: R_{abs}

3.4 Single muon selection

The cuts applied to the obtained muons are as follows:

- $-3.6 < \eta < -2.5$
- $17.5 \text{ cm} < R_{abs} < 89.5 \text{ cm}$
- $\text{pDCA} < 6\sigma$
- MFT-MCH matching $\chi^2 < 40$

The η cut is aligned with the MFT-MHC-MID acceptance. The R_{abs} cut value is set to exclude values that are influenced by the presence of the hadron absorber rear end. The pDCA is the product of momentum and DCA, and this cut is applied to remove muons originating from beam gas. Events with pDCA larger than 6σ when fitted with a Gaussian distribution are excluded. The final MFT-MCH matching χ^2 value is obtained from a fit using the detected points of the MFT and MCH tracks when matching them. The value used in this study is optimized, as described later, to maximize the statistical uncertainty of the yields for ω and ϕ . The distributions of the physical quantities of the single muons are provided below.

3.5 Dimuon analysis

3.5.1 Dimuon reconstruction

Using the single muons selected in 3.4, we reconstruct the dimuons. The mass, p_T , η , and ϕ of the dimuon are calculated as follows. First, we recalculate the p_x , p_y , p_z , and E from the single muon's p_T , η , and ϕ :

$$p_x = p_T \cos(\phi) \quad (28)$$

$$p_y = p_T \sin(\phi) \quad (29)$$

$$p_z = p_T \sinh(\eta) \quad (30)$$

$$E = \sqrt{p_T^2 \cosh^2(\eta) + m_\mu^2} \quad (31)$$

Then, using the p_x , p_y , p_z , and E of the single muon, the p_x , p_y , p_z , and E of the dimuon are calculated. Using the resulting four-momentum of the dimuon, the pair's $M_{\mu\mu}$, p_T , and η are computed from the following equations:

$$M_{\mu\mu} = \sqrt{E^2 - (p_x^2 + p_y^2 + p_z^2)} \quad (32)$$

$$p_{T\mu\mu} = \sqrt{p_x^2 + p_y^2} \quad (33)$$

$$\eta_{\mu\mu} = -\log \left(\tan \left(\frac{1}{2} \arctan \left(\frac{\sqrt{p_x^2 + p_y^2}}{p_z} \right) \right) \right) \quad (34)$$

Using the above formulas, the physical quantities of the dimuon are calculated. The dimuon is formed by pairing opposite-charge muons within each event. If multiple combinations are possible, we pair all possible combinations and reconstruct the dimuon's physical quantities. Since all possible combinations are considered, the mass distribution is also reconstructed for uncorrelated muon pairs. This is referred to as the combinatorial background. As will be described in the next section, this background can be statistically subtracted. Here is the English translation of your provided text:

3.5.2 Combinatorial background subtraction

Muons detected by the detector cannot be distinguished from which parent particle they originated. Therefore, when pairing muons, all μ^+ and μ^- pairs within each collision event are combined, and the mass is reconstructed. The uncorrelated mass distribution is estimated and subtracted afterward to leave only the mass distribution of correlated muon pairs for the analysis. In this study, the Like-sign method was used. The Like-sign method estimates the uncorrelated background events using the mass distribution of same-sign muon pairs obtained from the same event. The formula is as follows:

$$\frac{dN_{sig}}{dm} = \frac{dN_{same}^{+-}}{dm} - 2R\sqrt{\frac{dN_{same}^{++}}{dm}\frac{dN_{same}^{--}}{dm}} \quad (35)$$

$$2R = \frac{\frac{dN_{mix}^{+-}}{dm}}{\sqrt{\frac{dN_{mix}^{++}}{dm}\frac{dN_{mix}^{--}}{dm}}} \quad (36)$$

Here, $\frac{dN_{sig}}{dm}$ represents the number of correlated muons at each mass, $\frac{dN_{same}^{**}}{dm}$ represents the number of same-sign muon pairs in the same event (** corresponds to the muon sign), and $\frac{dN_{mix}^{**}}{dm}$ represents the number of muon pairs formed from different events. R is a term to correct for the acceptance difference due to the muon sign. If there is no acceptance difference due to the sign, R = 1. In this analysis, since muon pairs from different events were not combined, R = 1 was used for the calculation. The characteristic of the Like-sign method is that it subtracts uncorrelated background events using same-sign muon pairs from the same event. This allows for the subtraction of weakly correlated particle mass distributions within each event, such as those caused by elliptic flow in heavy-ion collisions. The uncorrelated background events estimated by the Like-sign method depend on the p_T of the dimuon. Therefore, the mass distributions were separated by the p_T of the dimuon, and for each invariant mass distribution, the uncorrelated background events were subtracted using the Like-sign method. The resulting subtracted plots are shown in Figures 15 to 20. The black line represents the distribution obtained by pairing muons with opposite charges within the same event and reconstructing the mass. The blue line represents the estimated uncorrelated background events using the Like-sign method. The red line represents the distribution obtained by subtracting the blue distribution from the black distribution, which corresponds to the correlated dimuon invariant mass distribution. In the $0 < p_T < 1$ GeV region, the MFT-MCH matching

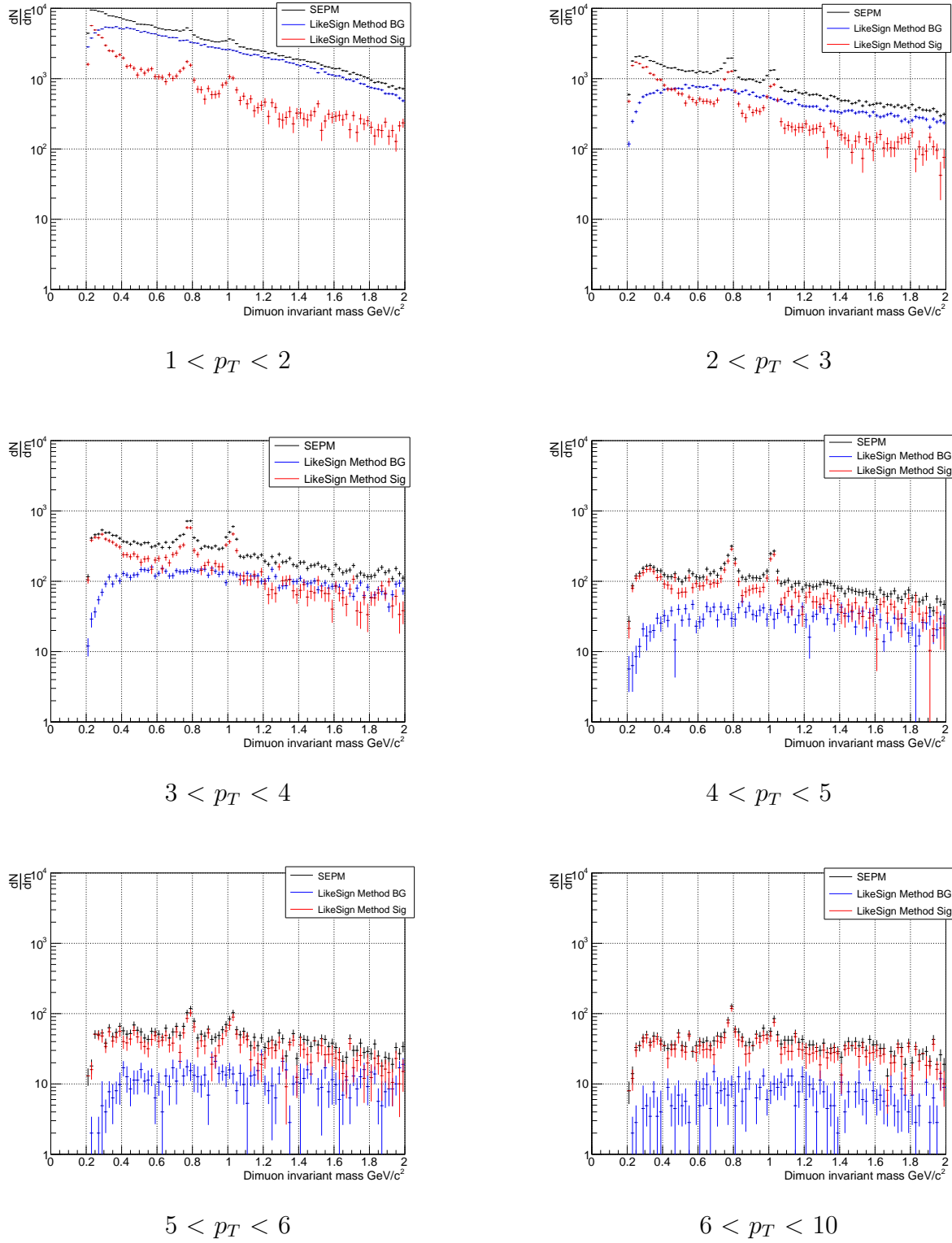


Figure 21: Results after subtracting uncorrelated background events in each p_T region

quality was insufficient, and no peaks for ω and ϕ were observed. The $6 < p_T < 10$ GeV region was taken wider than other transverse momentum regions to preserve the statistical significance.

3.5.3 Peak extraction of $\omega \rightarrow \mu\mu, \phi \rightarrow \mu\mu$

The distributions of the correlated dimuon invariant mass obtained from 3.5.2 are used to extract the distributions of $\omega \rightarrow \mu\mu, \phi \rightarrow \mu\mu$. Below 2GeV, the dimuon invariant mass distribution contains pairs of muons coming from light mesons and open charm:

- $\eta \rightarrow \mu^+ \mu^-$
- $\eta \rightarrow \mu^+ \mu^- \gamma$
- $\rho \rightarrow \mu^+ \mu^-$
- $\omega \rightarrow \mu^+ \mu^-$
- $\omega \rightarrow \mu^+ \mu^- \pi^0$
- $\eta' \rightarrow \mu^+ \mu^- \gamma$
- $\phi \rightarrow \mu^+ \mu^-$
- $c\bar{c} \rightarrow D\bar{D} \rightarrow \mu^+ \mu^- + others$
- $b\bar{b} \rightarrow B\bar{B} \rightarrow \mu^+ \mu^- + others$

The $\omega \rightarrow \mu\mu, \phi \rightarrow \mu\mu$ processes each have sharp peak structures, with peaks around 0.8GeV and 1.0GeV in the mass distribution. In this analysis, all distributions other than these are considered background events. Therefore, an exponential fit is performed to the continuous component of the mass distribution, and only the peaks are extracted. The fit function is as follows:

$$f(m) = N_0 * \exp\{-p1 * m\} + N_\omega * \exp\left\{-\frac{1}{2}\left(\frac{m - M_\omega}{\sigma_\omega}\right)^2\right\} + N_\phi * \exp\left\{-\frac{1}{2}\left(\frac{m - M_\phi}{\sigma_\phi}\right)^2\right\} \quad (37)$$

Here, $N_0, N_\omega, N_\phi, M_\omega, M_\phi, \sigma_\omega, \sigma_\phi$ are fit parameters, with M_ω and M_ϕ representing the mean mass positions of ω and ϕ , and σ_ω and σ_ϕ corresponding to the mass widths. This fit function was applied to the red correlated invariant mass distributions in 15–20. The results are shown in 22–27. The mean mass positions and mass widths for ω and ϕ , as well as the fit χ^2 values for each transverse momentum region, are summarized in the following table.

3.5.4 Yield calculation of ω, ϕ

Using the mean mass position and mass width of $\omega \rightarrow \mu\mu$ and $\phi \rightarrow \mu\mu$ obtained from the above fit, the yield for each meson was calculated. The number of dimuons falling within 3σ of each Gaussian was calculated as the yield for ω and ϕ , respectively.

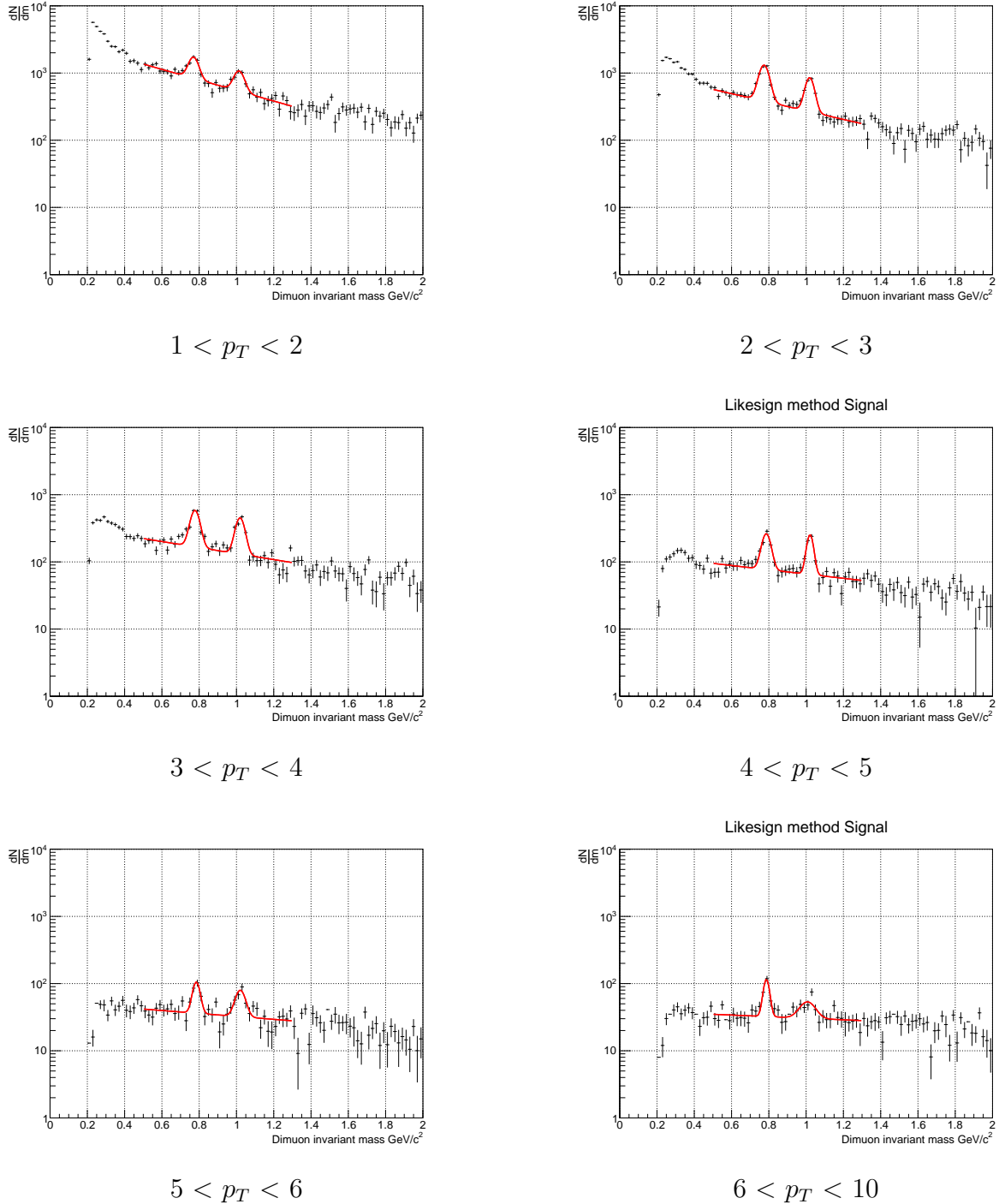


Figure 28: Results after subtracting uncorrelated background events in each momentum region.

Table 1: Fit Results

	ω mean mass	ω mass width	ϕ mean mass	ϕ mass width	fit χ^2
$1 < p_T < 2$					
$2 < p_T < 3$					
$3 < p_T < 4$					
$4 < p_T < 5$					
$5 < p_T < 6$					
$6 < p_T < 10$					

3.5.5 MFT-MCH matching χ^2 Optimization

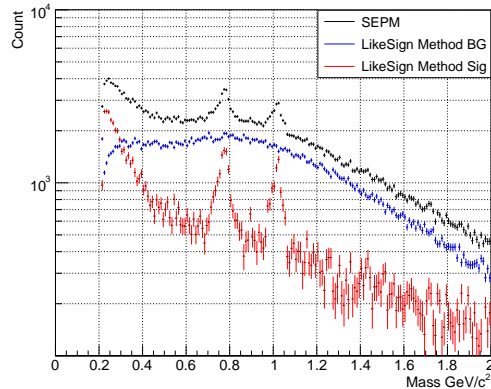
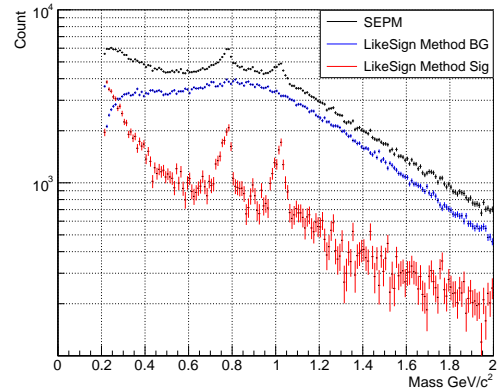
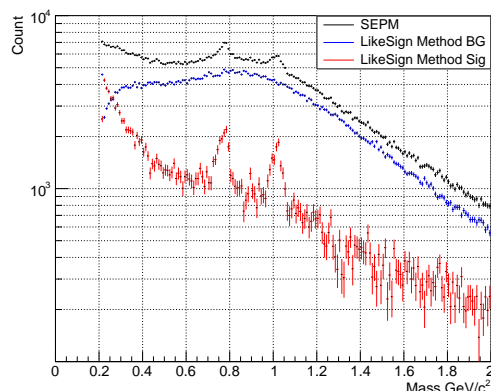
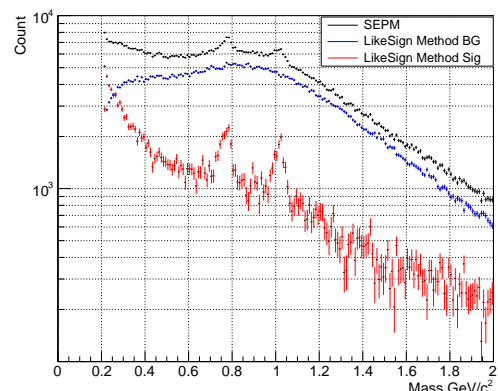
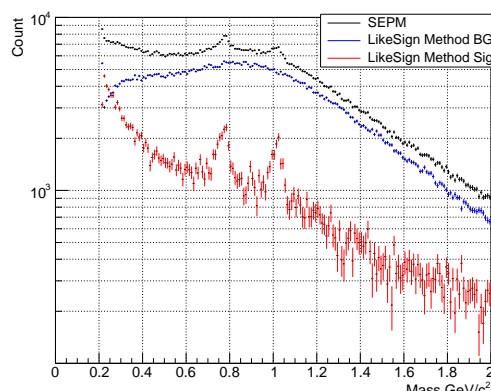
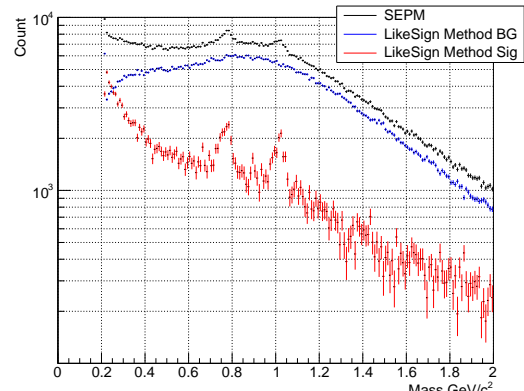
Using the yield analysis method for $\omega \rightarrow \mu\mu$ and $\phi \rightarrow \mu\mu$ as in 3.5.2, the optimization of the MFT-MCH matching χ^2 for the Single muon Track was performed. The MFT-MCH matching χ^2 is the χ^2 value obtained when matching the tracks from MFT and MCH, and large values are considered indicative of fake matches. This value was optimized such that the statistical error of each yield is minimized. First, the mass distribution was constructed using only muon tracks with an MFT-MCH matching $\chi^2 <$ value, and a fit was performed as described above. The results are shown in the figures below.

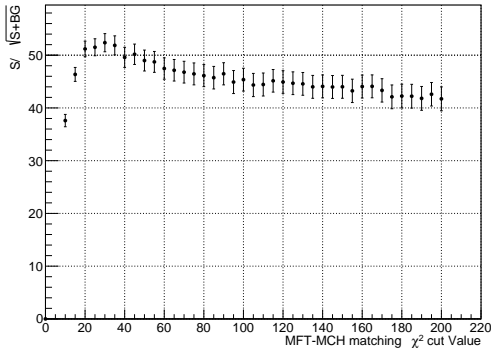
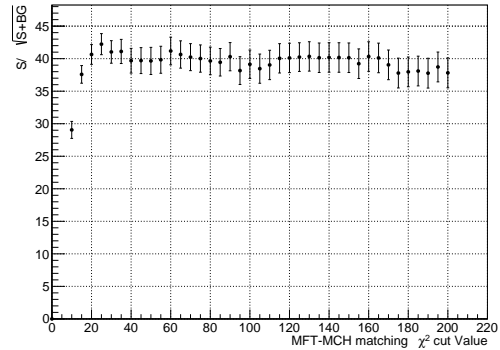
Similarly, from the fit results, the yields for $\omega \rightarrow \mu\mu$ and $\phi \rightarrow \mu\mu$ were obtained. These yields were then normalized by dividing by the number of dimuons in the same mass region, and the optimization was performed to maximize $S/\sqrt{S + BG}$. The resulting plot is shown below, where the x-axis is the matching χ^2 and the y-axis is $S/\sqrt{S + BG}$. From this, it is observed that the optimal value for the matching χ^2 is $\chi^2 < 35$.

3.6 Fake Match Track Removal Analysis of MFT-MCH-MID Track using MFT Track η - MCH Track η

The matching of MFT Tracks located before the hadron absorption pair and MCH Tracks located behind them is important for the quality of physical quantities such as single muon p_T and η . Here, we performed an analysis to remove MFT-MCH-MID tracks, which match incorrect tracks, by applying cuts to the already reconstructed Global Tracks using three detectors. The dataset used is LHC24b1, which is a Monte Carlo dataset for $pp\sqrt{s} = 13.6\text{TeV}$ minimum-bias events. This simulation data is detailed in ??.

The tracks reconstructed with MFT-MCH-MID tracks, as shown in 37, include tracks reconstructed outside the acceptance. The black histogram shows the η distribution of the reconstructed Global Tracks. Blue represents the η distribution of fake match tracks, and red represents the η distribution of correct match tracks. The green distribution corresponds to the true η distribution for the black tracks. By comparing the green and black distributions, we observe that muons outside the acceptance are reconstructed, and they form the distribution of fake matches. To remove such tracks, we applied the

MFT-MCH matching $\chi^2 < 20$ MFT-MCH matching $\chi^2 < 40$ MFT-MCH matching $\chi^2 < 60$ MFT-MCH matching $\chi^2 < 80$ MFT-MCH matching $\chi^2 < 100$ MFT-MCH matching $\chi^2 < 200$

Figure 35: ω figure of meritFigure 36: ϕ figure of merit

following $\Delta\eta$ cut:

$$\Delta\eta = \text{MFT } \eta - \text{MCH } \eta \quad (38)$$

We calculated $\Delta\eta$ for each track and examined the distributions of fake match tracks and correct match tracks. The resulting distributions are shown in the following figure, where blue represents the fake match distribution and red represents the correct match distribution. From 38, we see that for $\Delta\eta > 0.2$, fake match tracks dominate. To remove

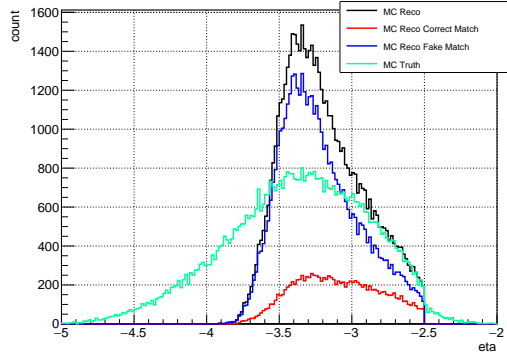
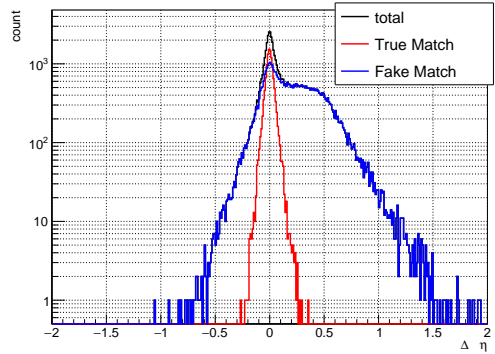
Figure 37: MFT-MCH-MID Track η 

Figure 38

fake matches while preserving as many correct matches as possible, we applied a $\Delta\eta < 0.2$ cut. The distributions of each physical quantity after this cut are as follows. In 39, all reconstructed tracks are shown in black, with red representing correct match tracks, blue representing fake match tracks, and green representing the true muon track distribution. By comparing the green distribution in 37, we observe that after the cut, tracks outside the acceptance have been removed. However, fake match tracks inside the acceptance remain. As shown in the p_T distribution, there are still many fake match tracks at low p_T . The resolution of each physical quantity is shown below. The horizontal axis shows the difference between the reconstructed values and the true values, divided by the true values, while the vertical axis represents the number of occurrences. The black histogram represents the resolution without applying the $\Delta\eta$ cut, and the red histogram represents

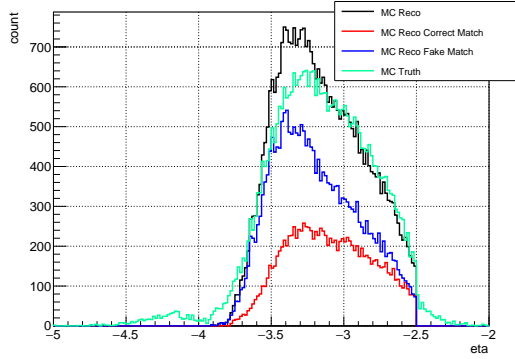


Figure 39: MFT-MCH-MID Track cutted η

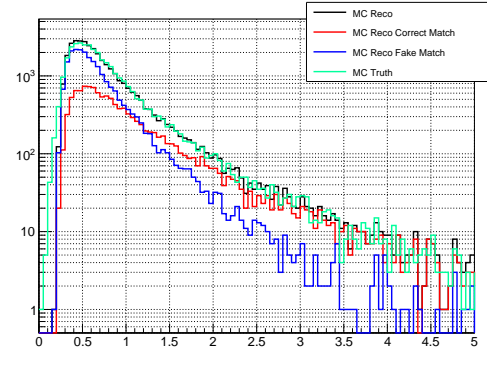


Figure 40: MFT-MCH-MID Track cutted p_T

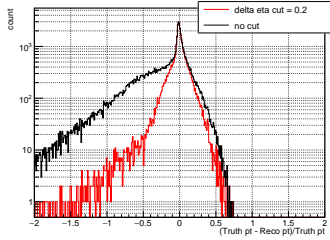


Figure 41: MFT-MCH- Figure 42: MFT-MCH- Figure 43: MFT-MCH-
MID Track cutted η MID Track cutted p_T MID Track cutted p_T

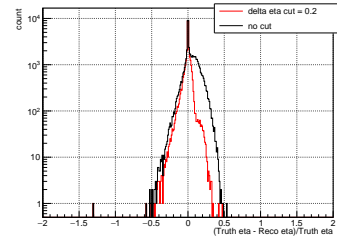


Figure 42: MFT-MCH- Figure 43: MFT-MCH- Figure 43: MFT-MCH-
MID Track cutted p_T MID Track cutted p_T MID Track cutted p_T

the tracks after applying the $\Delta\eta < 0.2$ cut. By comparing the black and red histograms, we can see that all distributions show improved resolution for single muons. Furthermore, efficiency and matching purity are provided below.

The chosen cut value ($\Delta\eta < 0.2$) was selected to discard only the fake match tracks while keeping the correct match tracks, so the efficiency is reduced, but the matching purity has improved. The efficiency \times purity value remains almost unchanged before and after the cut.

4 Results

This is the p_T spectrum of the yield for ω and ϕ . Since the cross section has not been calculated for the vertical axis yet, a comparison with other experimental results cannot be made. However, a distribution with an exponential dependence on p_T can be observed.

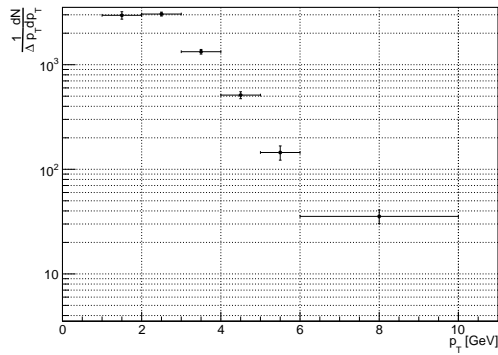


Figure 44: ω yield

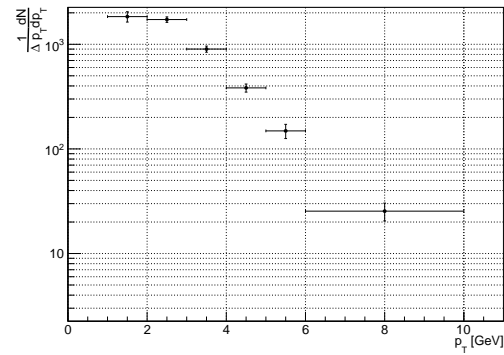


Figure 45: ϕ yield

References

- [1] S. Navas *et al.* [Particle Data Group], Phys. Rev. D **110**, no.3, 030001 (2024) doi:10.1103/PhysRevD.110.030001
- [2] W. Weise, Nucl. Phys. A **553**, 59C-72C (1993) doi:10.1016/0375-9474(93)90615-5
- [3] A. Maire, "Phase diagram of QCD matter: Quark-Gluon Plasma," 2015. Available at: <https://cds.cern.ch/record/2025215>
- [4] ALICE Collaboration., Acharya, S., Adamová, D. et al. The ALICE experiment: a journey through QCD. Eur. Phys. J. C **84**, 813 (2024). <https://doi.org/10.1140/epjc/s10052-024-12935-y>
- [5] F. Geurts and R. A. Tripolt, Prog. Part. Nucl. Phys. **128**, 104004 (2023) doi:10.1016/j.ppnp.2022.104004 [arXiv:2210.01622 [hep-ph]].
- [6] S. Acharya *et al.* [ALICE], [arXiv:2308.16704 [nucl-ex]].
- [7] R. Rapp and J. Wambach, Adv. Nucl. Phys. **25**, 1 (2000) doi:10.1007/0-306-47101-9_1 [arXiv:hep-ph/9909229 [hep-ph]].
- [8] S. Damjanovic *et al.* [NA60], Nucl. Phys. A **783**, 327-334 (2007) doi:10.1016/j.nuclphysa.2006.11.015 [arXiv:nucl-ex/0701015 [nucl-ex]].
- [9] "Technical Design Report for the Muon Forward Tracker," CERN-LHCC-2015-001, ALICE-TDR-018, 2015. Available at